Stereochemistry of Spiro-Acetalized [60]Fullerenes: How the *Exo* and *Endo* Stereoisomers Influence Organic Solar Cell Performance

Tsubasa Mikie,[†] Akinori Saeki,* Yu Yamazaki, Naohiko Ikuma, Ken Kokubo,* and Shu Seki*,[†]

Department of Applied Chemistry, Graduate School of Engineering, Osaka University, 2-1 Yamadaoka, Suita, Osaka 565-0871, Japan

Ⓢ *Supporting Information*

ABSTRACT: Exploiting bis-addition products of fullerenes is a rational way to improve the efficiency of bulk heterojunction-type organic photovoltaic cells (OPV); however, this design inherently produces regio- and stereoisomers that may impair the ultimate performance and fabrication reproducibility. Here, we report unprecedented *exo* and *endo* stereoisomers of the spiro-acetalized [60]fullerene monoadduct with methyl- or phenyl-substituted 1,3-dioxane (**SAF_6**). Although there is no chiral carbon in either the reagent or the fullerene, equatorial (*eq*) rather than axial (*ax*) isomers are selectively produced at

an *exo-eq:endo-eq* ratio of approximately 1:1 and can be easily separated using silica gel column chromatography. Nuclear Overhauser effect measurements identified the conformations of the straight *exo* isomer and bent *endo* isomer. We discuss the origin of stereoselectivity, the anomeric effect, intermolecular ordering in the film state, and the performance of poly(3-hexylthiophene):substituted **SAF_6** OPV devices. Despite their identical optical and electrochemical properties, their solubilities and space-charge limited current mobilities are largely influenced by the stereoisomers, which leads to variation in the OPV efficiency. This study emphasizes the importance of fullerene stereochemistry for understanding the relationship between stereochemical structures and device output.

KEYWORDS: bulk heterojunction, organic photovoltaic, stereoselectivity, stereoisomer, conformation
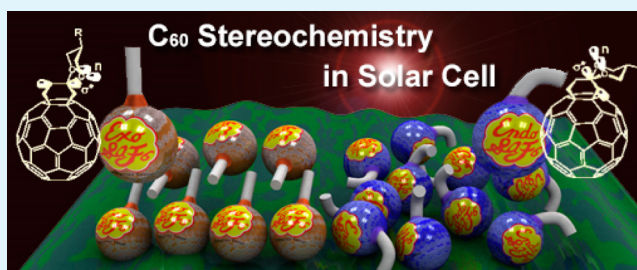
■ INTRODUCTION

Photoelectric conversion of sunlight is a promising technology for generating clean and safe energy. Light-weight and cost-effective organic photovoltaics (OPVs) have garnered intense attention as an alternative to expensive inorganic solar cells.[1−3] Bulk heterojunction (BHJ) frameworks, in particular, have evolved over the current decade, and the highest power conversion efficiency (PCE) is rapidly approaching the criterion for commercial application.[4] The blend of regioregular poly(3-hexylthiopene) (P3HT) and [6,6]-phenyl-C_{61}-butyric acid methyl ester (PCBM),[5−8] an early prototype of BHJ, has been followed by highly efficient low bandgap polymers (LBPs) to provide PCEs over 9−10%.[9−13]

As a counterpart of the p-type π-conjugated polymers, efforts have been devoted to the development of novel n-type fullerenes.[14−17] The use of [70]fullerene and/or the bis-adducts[18−22] is generally the most effective strategy toward enhancement of the short circuit current density (*J_{sc}*) and open-circuit voltage (*V_{oc}*). However, both designs inherently produce some regio-[23−27] and stereoisomers,[28−30] which can enhance their solubilities but in turn may deteriorate the PCE and fabrication reproducibility. Despite the success of bis-adduct fullerenes, such as indene C_{60} bis-adduct (ICBA) suitable for crystalline P3HT,[18] the mixture of fullerene regioisomers is often incompatible with efficient LBPs because of the excessive miscibility with polymers unable to form bicontinuous domains of pure substances.[31] Therefore, a stereochemically controlled

fullerene monoadduct without regioisomers is of importance for establishing a basis for the design of efficient OPVs; however, no such fullerene has been determined to date.

Recently, we reported that the 58π spiro-acetalized fullerene monoadduct **SAF_n** (*n* = 5−7 and denotes the size of acetal ring) is a vital platform for a polymer:fullerene OPV.[32] The PCE of 4.0% for this platform, which was comparable to the benchmark P3HT:PCBM (4.1%), has motivated attempts to append an additional substituent (methyl (Me) or phenyl (Ph)) at the para position of the spiro-acetal ring of **SAF_6** to improve the solubility (Scheme 1). The underlying concept of **MeSAF_6** and **PhSAF_6** is that there are no enantiomers due to the symmetrical diol reagent, which thus yields no regioisomers. However, the isomers can be equatorial (*eq*) or axial (*ax*), and we have determined that substituted **SAF_6** has two, *exo-eq* and *endo-eq*, out of the four possible stereoisomers (*exo-eq*, *endo-eq*, *exo-ax*, and *endo-ax*), of which contrasting conformations were identified by nuclear Overhauser effect (NOE) measurements. It should be emphasized that the selective preparation of *exo* and *endo* stereoisomers of the [60]fullerene monoadduct is unprecedented, except for those in which a chiral-carbon is directly introduced into the substituent.[33,34] Although the electrochemical properties of the stereoisomers were identical,

Scheme 1. TiCl$_4$-Mediated Acetalization of Cyclohexanone-Fused 1 with 2-R-1,3-propanediol (R = Methyl, Phenyl, or Dimethyl)

Figure 1. Differential NOE measurements of **MeSAF$_6$** stereoisomers with ^{1}H NMR spectroscopy.
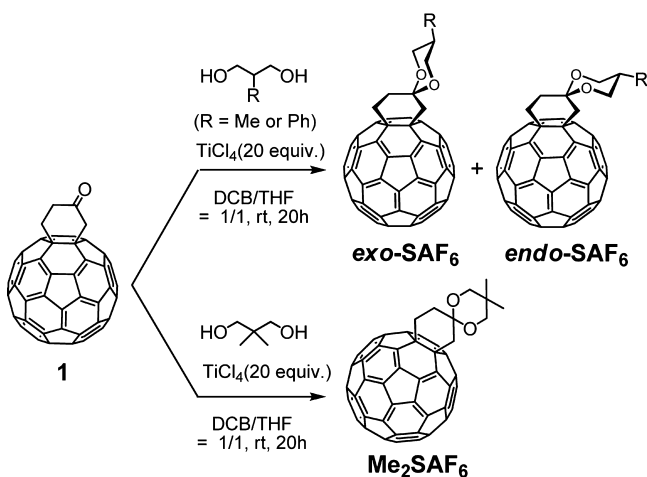
the different impacts of *exo* and *endo* isomers on the solubility, charge carrier mobility, intermolecular packing, and OPV performance are demonstrated clearly.

RESULTS AND DISCUSSION

The reactions of precursor **1** with 2-methyl-1,3-propanediol or 2-phenyl-1,3-propanediol were conducted in the presence of 20 equiv of TiCl$_4$ at room temperature according to the reported method,[35] which afforded **MeSAF$_6$** and **PhSAF$_6$** with high performance liquid chromatography (HPLC) yields of 99 and 91%, respectively (Scheme 1 and Table 1). **MeSAF$_6$** and

Table 1. Reaction Yields

compound	conv.[a] (%)	HPLC yield[b] (%)	ratio[c] (%)	isolated yield (%)	
				exo	*endo*
MeSAF$_6$	>99	99	59/41	50	35
PhSAF$_6$	95	91	54/46	48	33
Me$_2$SAF$_6$	89	89		85	

[a]Conversion of ketone **1**. [b]HPLC area yields of substituted **SAF$_6$**.
[c]*Exo-eq/endo-eq*

PhSAF$_6$ were confirmed to have two stereoisomers with a ratio of approximately 1:1 by HPLC analysis. The stereoisomers were easily separated by silica gel column chromatography and characterized using ^{1}H nuclear magnetic resonance (NMR) spectroscopy (Supporting Information Figures S1−S5) and differential NOE measurements (Figure 1 and Supporting Information Figures S6−S8).

In the NOE spectrum of *exo*-**MeSAF$_6$** (Supporting Information Figure S6a), a positive signal assigned to the protons of the spiro-acetalized unit (3.87 ppm, H$_{ax}$ in Figure 1) appeared under the selective irradiation of the protons at the fused cyclohexane (∼3.18 ppm), indicative of the interaction among these protons (red arrow in Figure 1). Thus, the structure was identified as the *exo* isomer. In the same fashion, the structure of the *endo* isomer was identified from the interaction between protons at 3.94 and 3.84 ppm (Supporting Information Figure S6b). Notably, the equatorial rather than axial isomers are selectively generated in both *exo/endo* isomers, where the acetal ring is away from and close to the fullerene
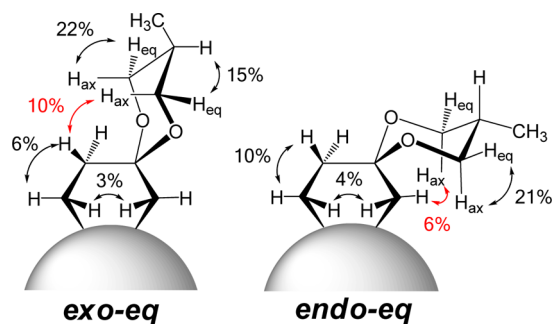
cage, respectively. The situation was similar in **PhSAF$_6$** (Supporting Information Figures S7 and S9). In stark contrast, dimethyl-substituted **Me$_2$SAF$_6$** was identified as a mixture of equatorial and axial conformers (Supporting Information Figures S8 and S10).

A plausible mechanism for the stereoselectivity is presented in Figure 2. The attack of compound **1** by the prochiral substituted-diol, mediated by the Ti catalyst, yields two racemic hemiacetal intermediates of (R*, R*) and (S*, R*) diastereomers. Subsequent cyclization of these diastereomers leads to the *exo* isomer from (R*, R*) and *endo* isomer from (S*, R*) via the upper side attack (the lower side attack is sterically unfavorable). Although it is possible to reverse the cyclic acetalization mediated by the Ti catalyst, the presence of excessive TiCl$_4$ (20 equiv in Scheme 1) removes H$_2$O to shift the equilibrium to the right side (Figure 2).[35] Therefore, the production of stereoisomers is presumed to be irreversible and determined mostly by the first attachment of the diol reagent hydroxyl unit to the side. This reaction is assumed to occur randomly, thus producing an approximate 1:1 ratio of *exo* and *endo* isomers (Table 1). The slight deviation from 1:1 yield is discussed below from the thermodynamic aspect of hemi-acetal intermediates.

Interestingly, the diastereomers afforded only one equatorial isomer despite the possibility of two conformational isomers (equatorial and axial). Density functional theory (DFT) calculations for **MeSAF$_6$** indicated that the *exo-eq* isomer is energetically more favored than the *endo-ax* isomer by 3.85 kJ mol^{-1} (Figure 2). Similarly, the *endo-eq* isomer is more favored than the *exo-ax* isomer by 4.32 kJ mol^{-1}. The more equatorial isomer being more stable than the axial one is due to the nonbonded interaction between the lone pairs of oxygen and Me (Figure 2). This is in good agreement with the observed majority of equatorial isomers in both *exo* and *endo* isomers. However, when comparing equatorial isomers (*exo-eq* and *endo-eq*), the former is unstable by 1.68 kJ mol^{-1} compared to the latter, which is not consistent with the almost equal yield obtained. Instead, the yield is slightly higher for the *exo-eq* than the *endo-eq* isomer (59:41 for **MeSAF$_6$**, Table 1). This can be rationalized by energetic consideration of the hemiacetal intermediates, where the *exo-eq* precursor (R*, R*) is 0.46 kJ mol^{-1} more stable than the *endo-eq* precursor (S*, R*), which suggests that the stabilities of intermediates rather than just those of products also impact the yield ratio of *exo/endo*. In addition to the flipping motion of the twist-boat conformation of compound **1**, the activation energies between compound **1**, intermediate, and products associated with the stabilities of the intermediates may also deviate the yield ratio toward the *exo*
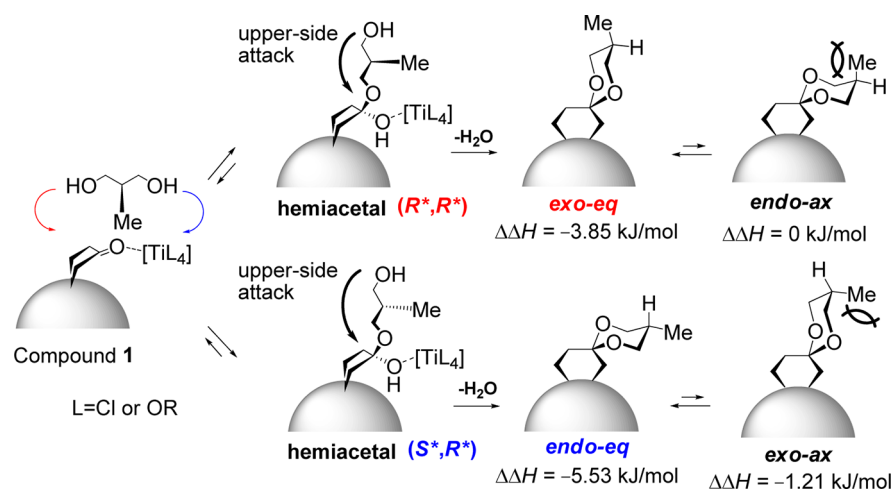
Figure 2. Plausible reaction mechanism and $\Delta\Delta H$ for four possible stereoisomers of **MeSAF$_6$** relative to *endo-ax* calculated by the DFT method with B3LYP/6-31G*, where *eq* and *ax* represent equatorial and axial conformers, respectively.

isomer side. Therefore, both kinetically controlled and thermodynamically controlled reactions cooperatively govern the yield ratio of *exo/endo* isomers. In light of the mostly equal yield and the presence of excessive TiCl$_4$ to shift the equilibrium, kinetic factors are assumed to be more dominant than thermodynamic ones.

In sharp contrast to the clear stereoselectivity in **MeSAF$_6$** and **PhSAF$_6$**, a mixture of *exo* and *endo* isomers was observed in **Me$_2$SAF$_6$**. In this case, the structures undergo a flip between *exo* and *endo* conformations, as dictated by NOE. DFT calculations of *exo*- and *endo*-**Me$_2$SAF$_6$** indicate a total energy for the *endo* isomer that is 0.66 kJ mol^{-1} smaller than that for the *exo* isomer, which is sufficiently small to flip the conformation at room temperature. The more stable *endo* than *exo* isomer in **Me$_2$SAF$_6$** is understood to be subject to the electron-withdrawing nature of C$_{60}$ that stabilizes a hybridized molecular orbital comprising the lone pair of the oxygen atom and σ^* orbital of the closest C−C bond (Supporting Information Figure S11). This is analogous to, but not exactly the same as, the anomeric effect that is well documented for pyran and dioxane.[36−39]

The lowest unoccupied molecular orbital (LUMO) levels of substituted **SAF$_6$** derivatives were measured using cyclic voltammetry (Supporting Information Figure S12), and the results are listed in Table 2. All compounds exhibited three reduction waves, and the LUMO levels of −3.59 eV (**MeSAF$_6$** and **Me$_2$SAF$_6$**) and −3.60 eV (**PhSAF$_6$**) are identical to that of nonsubstituted **SAF$_6$** (−3.59 eV).[32] The LUMOs are slightly shallower than PCBM (−3.63 eV) due to the electron-donating nature of the acetal unit. The electrostatic potentials (ESP) of

SAF$_6$ and PCBM calculated by DFT support this claim, demonstrating that a larger extent of electron density flows into the fullerene cage for **SAF$_6$** than PCBM (Supporting Information Figure S13).[40] Regarding the UV−vis photoabsorption spectra, there are no differences in **MeSAF$_6$**, **Me$_2$SAF$_6$**, and **PhSAF$_6$** (Supporting Information Figure S14). Despite the same LUMO levels and photoabsorption, the solubilities in toluene are quite different between the stereoisomers. The *endo* isomers have much higher solubility (2.3−2.5 wt %) than *exo* isomers (1.3−1.4 wt %), irrespective of the substituents (Me or Ph). The solubility of **Me$_2$SAF$_6$** (1.5 wt %) is between that for the *exo* and *endo* isomers in accordance with the mixed structure determined by NOE.

The intermolecular packing of *exo*-**PhSAF$_6$** was determined by X-ray diffraction (XRD) analysis.[41] A single crystal of *exo*-**PhSAF$_6$** was obtained by slow evaporation of the solvent mixture of chloroform (CDCl$_3$) and carbon disulfide (CS$_2$) from a solution with a stoichiometry of *exo*-**PhSAF$_6$**:CDCl$_3$:CS$_2$ = 1:1:1. The other **SAF$_6$** derivatives yielded only fine powders unsuitable for single-crystal XRD analysis. Figure 3 shows that the long straight substituents of *exo*-**PhSAF$_6$** are arranged in a way to intercalate into the *a*-axis fullerene packing, thereby forming a layer-like structure. The structure is in good agreement with the NOE observation (Figure 1). The unique stick-ball shape causes variation in the center-to-center distances of fullerene ($d_{c\text{-}c}$) packing in the range of 10.18, 13.40, and 17.30 Å along the *a*, *b*, and *c* axes, respectively. This relatively large anisotropic packing (∼1.70) is contrary to the previous nonsubstituted spiro-thioacetalized fullerene (**STAF$_8$**), where $d_{c\text{-}c}$ were 9.98, 10.07, and 10.09 Å along the *a*, *b*, and *c* axes, respectively,[32] thereby leading to isotropic packing (∼1.01).

Two-dimensional grazing-incidence XRD (2D-GIXRD) measurements indicated diffraction for *exo*-**MeSAF$_6$** (Figure 4a) that was more sharp and intense than that for *endo*-**MeSAF$_6$** (Figure 4b), which corroborates the high crystallinity of the former. The averaged radial profiles shown in Figure 4c clearly resolve the single peak for *exo*-**MeSAF$_6$** at q = 1.36 Å^{-1} (*d*-spacing of 4.63 Å) along with three shoulders (values listed in Supporting Information Table S2). In contrast, *endo*-**MeSAF$_6$** accompanies two weak peaks at 4.65 and 4.49 Å over the dominant broad diffraction. Although the *d*-spacing of these fullerenes are similar to that of PCBM (4.64 Å),[42] the full

Table 2. Electrochemical Properties and Solubilities

compound	E^1_{red} (V)[a]	LUMO (eV)[b]	solubility (wt %)[c]
exo-MeSAF$_6$	−1.21	−3.59	1.3
endo-MeSAF$_6$	−1.21	−3.59	2.3
exo-PhSAF$_6$	−1.20	−3.60	1.4
endo-PhSAF$_6$	−1.20	−3.60	2.5
Me$_2$SAF$_6$	−1.21	−3.59	1.5
PCBM[d]	−1.17	−3.63	1.0

[a]The first reduction wave in DCB. [b]Calculated by LUMO = −e(4.8 + E^1_{red}). [c]In toluene. [d]Taken from ref 32.
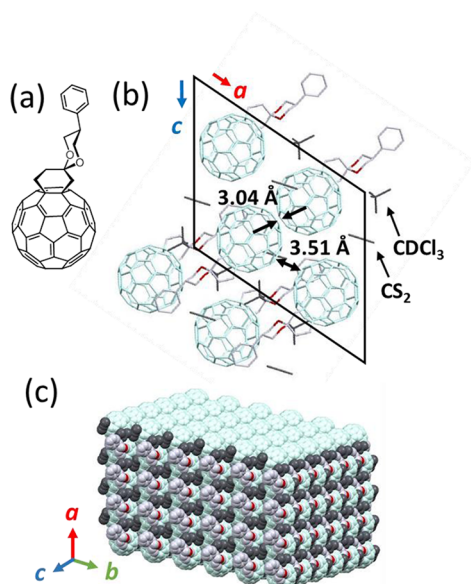
Figure 3. (a) Chemical structure and drawings of ***exo*-PhSAF$_6$**. (b) Diagram of unit cell. CDCl$_3$ and CS$_2$ solvents are depicted in black. (c) Packing structure using the space-filling model.
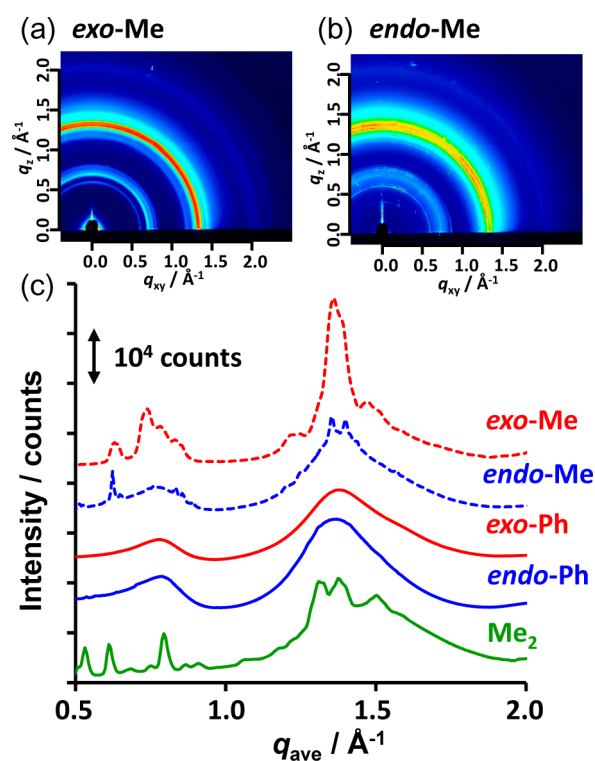

Figure 4. 2D-GIXRD images of pristine (a) ***exo*-MeSAF$_6$** and (b) ***endo*-MeSAF$_6$** films prepared by drop-casting from the DCB solutions. The films were subjected to thermal annealing at 150 °C for 10 min. (c) Radial profiles averaged from 10° to 80°.

width at half-maximum (fwhm) of the 2θ plot for ***endo*-MeSAF$_6$** is approximately three times larger than that for ***exo*-MeSAF$_6$** (Supporting Information Table S2), indicating fragmentation of the crystallite and a less crystalline nature of the ***endo*-MeSAF$_6$**. Notably, the XRD profile of **Me$_2$SAF$_6$** is a superposition of ***exo*-MeSAF$_6$** and ***endo*-MeSAF$_6$** comprising three peaks with the broad spectrum, which is consistent with

the allowed flipping between the *exo* and *endo* conformation of **Me$_2$SAF$_6$**. Furthermore, the crowded diffraction pattern of **Me$_2$SAF$_6$** is suggestive of variation in the crystalline forms, such as an *exo*-rich part, an *endo*-rich part, and the *exo*-*endo* mixture. On the contrary, both ***exo*-PhSAF$_6$** and ***endo*-PhSAF$_6$** display broad spectra without sharp peaks (Supporting Information Figure S15). Despite the formation of a single cocrystal of ***exo*-PhSAF$_6$:CDCl$_3$:CS$_2$** (Figure 3), the ***exo*-PhSAF$_6$** film processed from *o*-dichlorobenzene (DCB) did not effectively form crystallites. The slightly shortened *d*-spacing of ***exo*-PhSAF$_6$** (4.55 Å) might be a signature of its closer packing than that of ***endo*-PhSAF$_6$** (4.59 Å), even though their fwhms were mostly equal.

Accordingly, the expected packing of *exo* and *endo* isomers (mainly **MeSAF$_6$**) in the film state are illustrated in Figure 5.
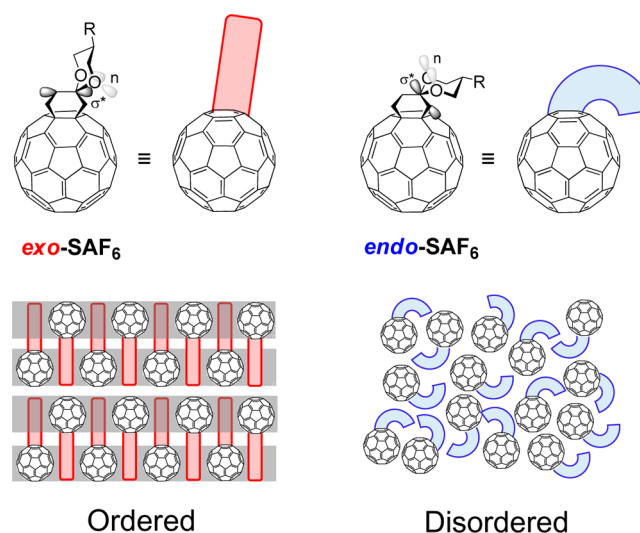
Figure 5. Schematic of intermolecular packing of *exo* and *endo* isomers. R = Me or Ph (mainly Me).

The *exo* isomers can form ordered structures that are beneficial to electron transport, whereas the packing of *endo* isomers is inhibited by the bending conformation of the substituents that wrap around the fullerene cage, which could lead to a rather disordered molecular arrangement in the film state. These aspects correspond to the higher solubility of the *endo* isomers than that of the *exo* isomers.

The OPV performances of P3HT:substituted **SAF$_6$** (1:1 w/w) were evaluated for a typical cell of ITO/PEDOT:PSS/BHJ (200 nm thick)/Ca/Al fabricated according to a previously reported procedure.[43] The thermal annealing temperatures were optimized for all of the devices (120 °C for **Me$_2$SAF$_6$**, 150 °C for ***exo*-SAF$_6$**, and 170 °C for ***endo*-SAF$_6$**, Supporting Information Table S3 and Figure S16). Figure 6 shows the current density versus voltage (J−V) characteristics under AM 1.5 G illumination at 100 mW cm^{-2}. The respective device parameters are listed in Table 3. ***Exo*-PhSAF$_6$** recorded the best PCE of 3.53% (average: 3.49 ± 0.04%) with a V_{oc} of 0.63 V, J_{sc} of 8.01 mA cm^{-2}, and a fill factor (FF) of 0.71. The most comparable PCE of 3.50% (average: 3.46 ± 0.04%) was obtained for ***exo*-MeSAF$_6$** (V_{oc} = 0.65 V, J_{sc} = 7.52 mA cm^{-2}, FF = 0.71). In contrast, it is worth noting that the *endo* isomers (***endo*-PhSAF$_6$** and ***endo*-MeSAF$_6$**) resulted in a decrease of the PCEs at 3.11% (average: 3.02 ± 0.09%) and 3.23% (average: 3.14 ± 0.09%), respectively, which was ascribed to suppression
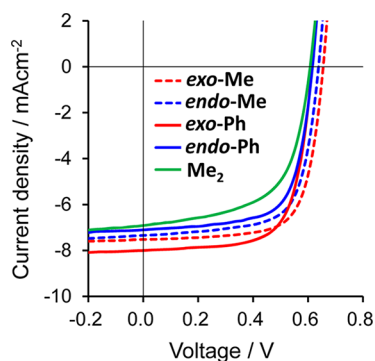
Figure 6. J−V curves for P3HT:fullerene (1:1 w/w) devices under AM 1.5 G (100 mW cm^{-2}).

**Table 3. OPV Performance under AM 1.5 G (100 mW cm^{-2})**

entry[a]	J_{sc} (mA cm^{-2})	V_{oc} (V)	FF	PCE (average)[f] (%)
P3HT:exo-MeSAF$_6$[b]	7.52	0.65	0.71	3.50 (3.46 ± 0.04)
P3HT:endo-MeSAF$_6$[c]	7.35	0.64	0.69	3.23 (3.14 ± 0.09)
P3HT:exo-PhSAF$_6$[b]	8.01	0.63	0.71	3.53 (3.49 ± 0.04)
P3HT:endo-PhSAF$_6$[c]	7.13	0.64	0.69	3.11 (3.02 ± 0.09)
P3HT:Me$_2$SAF$_6$[d]	6.94	0.63	0.60	2.63 (2.58 ± 0.05)
P3HT:SAF$_6$[e]	8.36	0.60	0.56	2.79 (2.53 ± 0.26)
P3HT:PCBM[b,e]	10.10	0.58	0.69	4.07 (4.01 ± 0.06)

[a]P3HT:fullerene = 1:1 in wt % processed from DCB (ITO/PEDOT:PSS/active layer/Ca/Al). [b]Annealed at 150 °C for 10 min. [c]Annealed at 170 °C for 10 min. [d]Annealed at 120 °C for 10 min. [e]Taken from ref 32. [f]Averaged over three devices.

of J_{sc} and FF. Therefore, PCEs of *exo*-SAF$_6$ (3.5%) are statistically higher than those of *endo*-SAF$_6$ (3.1−3.2%). Me$_2$SAF$_6$ showed the lowest PCE of 2.63% (average: 2.58 ± 0.05%) due to inefficient intermolecular packing from steric effects and the unfixed conformation of *exo* and *endo*. The situation was the same for nonsubstituted SAF$_6$ (PCE = 2.79%, average: 2.53 ± 0.26%).[32] All of the substituted SAF$_6$ isomers have excellent V_{oc}s (0.63−0.65 V) and FFs (0.60−0.71) among the fullerene monoadducts, although the PCEs (mainly J_{sc}s) are inferior to the reference P3HT:PCBM (PCE = 4.07%, average: 4.01 ± 0.06%).[32]

The plot of PCE for P3HT:fullerene monoadduct against solubility shown in Figure 7a has a convex curve with a maximum at ∼1.0 wt %, where the lower and higher solubility regions consist of the nonsubstituted S(T)AF$_n$ (previous work[32]) and substituted SAF$_6$ (present work), respectively. A similar convex trend has been reported for other fullerene derivatives.[44] Atomic force microscopy (AFM) observations indicated that there were no significant differences in the surface morphology or roughness (R_a = 4−7 nm) of the blends (Supporting Information Figure S17) or pristine fullerene films (R_a = 0.2−0.3 nm, Supporting Information Figure S18). Therefore, the electron mobility is intimately associated with the bulkiness of the solubilizing substituent, and the resultant fullerene packing is considered to have a large impact on the device performance.

The charge carrier mobilities of the P3HT:substituted SAF$_6$ blend film were investigated using the space-charge limited current (SCLC) technique.[45−47] Table 4 summarizes the hole
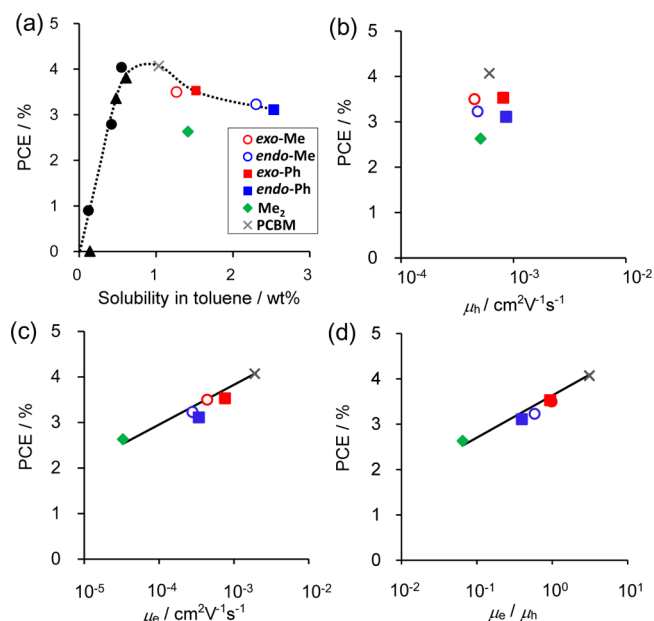
Figure 7. (a) PCE versus solubility of the fullerene in toluene. The solid black circles and triangles represent SAF$_n$ and STAF$_n$, respectively, taken from ref 32. Data for P3HT:PCBM were taken from ref 32. (b−d) PCE versus logarithmic plots of SCLC (b) hole mobility (μ_h), (c) electron mobility (μ_e), and (d) their balance (μ_e/μ_h).

Table 4. SCLC Hole and Electron Mobilities and Their Balance in P3HT:Fullerene Films

acceptor	μ_h (cm^2 V^{-1} s^{-1})	μ_e (cm^2 V^{-1}s^{-1})	μ_e/μ_h
exo-MeSAF$_6$	4.5×10^{-4}	4.4×10^{-4}	0.98
endo-MeSAF$_6$	4.8×10^{-4}	2.8×10^{-4}	0.58
exo-PhSAF$_6$	8.1×10^{-4}	7.6×10^{-4}	0.94
endo-PhSAF$_6$	8.6×10^{-4}	3.4×10^{-4}	0.40
Me$_2$SAF$_6$	5.1×10^{-4}	3.3×10^{-5}	0.06

mobility (μ_h), electron mobility (μ_e), and their ratio (μ_e/μ_h) exemplified in the blend films under OPV-optimized conditions (Supporting Information Figure S19). All of the P3HT:fullerene devices exhibit similar μ_h within a factor of 2 ((4.5−8.6) × 10^{-4} cm^2 V^{-1} s^{-1}), which indicates that there is no correlation with the PCE (Figure 7b). In sharp contrast, the μ_e varied by a factor of 23 ((0.33−7.6) × 10^{-4} cm^2 V^{-1} s^{-1}), which notably demonstrates a clear positive correlation with the PCE (Figure 7c). The plot of PCE as a function of μ_e/μ_h provides further evidence for the correlation (Figure 7d), which underscores the importance of mobility balance governing the overall PCE of OPV devices. This result is consistent with the simulation[48] and previous P3HT:S(T)AF$_n$ studies,[32] iterating that control of fullerene sterrerochemistry is a key for improving the OPV device performance. Although the *endo* isomers have higher solubility than the *exo* isomers, both the electron mobilities and the mobility balance were degraded due to the wrapping conformation, which inhibits tight and ordered intermolecular packing. Therefore, the mobility balance related to the conformation of the stereoisomers was determined to be a more dominant factor than the solubility in influencing performance.

CONCLUSION

We have elucidated for the first time how the stereochemistries of the *exo-eq* and *endo-eq* isomers of substituted **SAF$_6$** influence self-assembly in the bulk film and the resultant performances of P3HT-based OPV devices. The almost equal yield of the *exo* and *endo* isomers was explained by the kinetically controlled reaction mediated by excess Ti catalyst, and the selective generation of equatorial conformers rather than axial ones was rationalized by the thermodynamic stabilities of hemiacetal intermediates and products. Despite the identical electrochemical properties, the *exo* isomers with a straight substituent exhibit lower solubility than the *endo* isomers with a bent substituent. However, *exo*-**SAF$_6$** demonstrated a PCE (3.5%) superior to that of *endo*-**SAF$_6$** (3.1−3.2%) due to the higher electron mobility associated with the intercalating packing nature of the *exo* isomers. This work highlights the importance of rendering stereochemistry to extend the freedom of the fullerene design and provides perspective to achieve a deeper understanding of the structure−property relationships of polymer:fullerene OPVs.

EXPERIMENTAL SECTION

Materials, Synthesis, and Characterization. *Exo-* and *endo-***MeSAF$_6$**, *exo-* and *endo-***PhSAF$_6$**, and **Me$_2$SAF$_6$** were synthesized by following previous reports.[32,35] They were characterized by 400 MHz ^{1}H and 150 MHz ^{13}C NMR, differential NOE measurements, and MALDI-TOF-MS spectroscopy. Reduction potentials E^1_{red} standardized by Fc/Fc$^+$ coupling were evaluated by cyclic voltammetry in DCB using an Ag/AgCl electrode and Pt as the working and counter electrode, respectively. The LUMO levels were calculated from E^1 using LUMO level = $-e(E^1_{red} + 4.8)$. A single-crystal XRD experiment was conducted using a Rigaku RAXIS RAPID imaging plate area detector with graphite monochromated Cu K$_\alpha$ radiation. The 2D-GIXRD experiments were conducted at the SPring-8 (Japan Synchrotron Radiation Research Institute, JASRI) on the beamline BL46XU using 12.39 keV (λ = 1 Å) X-ray. The GIXRD patterns were recorded with a 2D image detector (Pilatus 300 K).

Organic Photovoltaic Cell (OPV). P3HT and *exo-* and *endo-***MeSAF$_6$**, *exo-* and *endo-***PhSAF$_6$**, and **Me$_2$SAF$_6$** were dissolved in DCB at a 1:1 wt ratio (1.5 wt %, 19.5 mg/mL for each). A PEDOT:PSS layer was cast onto the cleaned ITO layer by spin-coating after passing through a 0.45 μm filter. The substrate was annealed on a hot plate at 120 °C for 10 min. After the substrate was annealed on a hot plate at 180 °C for 10 min, the DCB solution was then cast on top of the PEDOT:PSS buffer layer in a nitrogen glovebox by spin-coating at 1400 rpm for 15 s after passing through a 0.2 μm filter. The active layer was thermal annealed upon 120, 150, and 170 °C for P3HT:**Me$_2$SAF$_6$**, *exo*-**SAF$_6$**, and *endo*-**SAF$_6$**, respectively. A cathode consisting of 20 nm Ca and 100 nm Al layers was sequentially deposited through a shadow mask on top of the active layers by thermal evaporation in a vacuum chamber. The resulting device configuration was ITO (120−160 nm)/PEDOT:PSS (45−60 nm)/active layer (∼200 nm)/Ca (20 nm)/Al (100 nm) with an active area of 7.1 mm^2. Current−voltage (J−V) curves were measured using a source-measure unit (ADCMT Corp., 6241A) under AM 1.5 G solar illumination at 100 mW cm^{-2} (1 sun, monitored by a calibrated standard cell, Bunko Keiki SM-250 KD) from a 300 W solar simulator (SAN-EI Corp., XES-301S). Atomic force microscopy (AFM) observations were performed by a Seiko Instruments Inc. model Nanocute OP and Nanonavi II.

Space-Charge Limited Current (SCLC). The device structures of SCLC were the ITO/PEDOT:PSS/active layer (∼200 nm)/Au for hole and Al/Active layer (∼230 nm)/LiF/Al for electron. The other procedures are same as the OPV device fabrication. The active layer (blend of P3HT and fullerene) was prepared under the optimized conditions. The hole or electron mobility was determined by fitting the J−V curve into the Mott−Gurney law ($J = 9\varepsilon_r\varepsilon_0\mu V^2/(8d^3)$), where

ε_0 is the permittivity of free space, ε_r is the relative dielectric constant of the material, μ is the hole (or electron) mobility, V is the voltage, and d is the layer thickness.[45−47]

ASSOCIATED CONTENT

Ⓢ Supporting Information

Compound data, crystallographic data, Figures S1−S19, Tables S1−S3, and CIF files. This material is available free of charge via the Internet at http://pubs.acs.org.

AUTHOR INFORMATION

Corresponding Authors
*E-mail: saeki@chem.eng.osaka-u.ac.jp.
*E-mail: kokubo@chem.eng.osaka-u.ac.jp.
*E-mail: seki@chem.eng.osaka-u.ac.jp.

Present Address
†Department of Molecular Engineering, Graduate School of Engineering, Kyoto University, A4-009 Kyoto University Katsura Campus, Nishikyo-ku, Kyoto 615-8510, Japan. Tel/Fax: +81-75-383-2572, E-mail: seki@moleng.kyoto-u.ac.jp.

Notes
The authors declare no competing financial interests.

ACKNOWLEDGMENTS

REFERENCES

(1) Arias, A. C.; Mackenzie, J. D.; McCulloch, I.; Rivnary, J.; Salleo, A. Materials and Applications for Large Area Electronics: Solution-Based Approaches. *Chem. Rev.* **2010**, *110*, 3−24.

(2) Janssen, R. A. J.; Nelson, J. Factors Limiting Device Efficiency in Organic Photovoltaics. *Adv. Mater.* **2013**, *25*, 1847−1858.

(3) Dimitrov, S. D.; Durrant, J. R. Materials Design Considerations for Charge Generation in Organic Solar Cells. *Chem. Mater.* **2014**, *26*, 616−630.

(4) Green, M. A.; Emery, K.; Hishikawa, Y.; Warta, W.; Dunlop, E. D. Solar Cell Efficiency Tables (Version 45). *Prog. Photovoltaics* **2015**, *23*, 1−9.

(5) Li, G.; Shrotriya, V.; Huang, J.; Yao, Y.; Moriarty, T.; Emery, K.; Yang, Y. High-Efficiency Solution Processable Polymer Photovoltaic Cells by Self-Organization of Polymer Blends. *Nat. Mater.* **2005**, *4*, 864−868.

(6) Kim, Y.; Cook, S.; Tuladhar, S. M.; Choulis, S. A.; Nelson, J.; Durrant, J. R.; Bradley, D. C.; Giles, M.; McCulloch, I.; Ha, C. S.; Ree, M. A Strong Regioregularity Effect in Self-Organizing Conjugated Polymer Films and High-Efficiency Polythiophene:Fullerene Solar Cells. *Nat. Mater.* **2006**, *5*, 197−203.

(7) Ma, W.; Yang, C.; Gong, X.; Lee, K.; Heeger, A. J. Thermally Stable, Efficient Polymer Solar Cells with Nanoscale Control of the Interpenetrating Network Morphology. *Adv. Funct. Mater.* **2005**, *15*, 1617−1622.

(8) Dang, M. T.; Hirsch, L.; Wantz, G. P3HT:PCBM, Best Seller in Polymer Photovoltaic Research. *Adv. Mater.* **2011**, *23*, 3597−3602.

(9) Guo, X.; Zhou, N.; Lou, S. J.; Smith, J.; Tice, D. B.; Hennek, J. W.; Ortiz, R. P.; Navarrete, J. T. L.; Li, S.; Strzalka, J.; Chen, L. X.; Chang, R. P. H.; Facchetti, A.; Marks, T. J. Polymer Solar Cells with Enhanced Fill Factors. *Nat. Photonics* **2013**, *7*, 825−833.

(10) Nguyen, T. L.; Choi, H.; Ko, S.-J.; Uddin, M. A.; Walker, B.; Yum, S.; Jeong, J.-E.; Yun, M. H.; Shin, T. J.; Hwang, S.; Kim, J. Y.;

Woo, H. Y. Semi-Crystalline Photovoltaic Polymers with Efficiency Exceeding 9% in a ~300 nm Thick Conventional Single-Cell Device. *Energy Environ. Sci.* **2014**, *7*, 3040−3051.

(11) Kong, J.; Hwang, I.-W.; Lee, K. Top-Down Approach for Nanophase Reconstruction in Bulk Heterojunction Solar Cells. *Adv. Mater.* **2014**, *26*, 6275−6283.

(12) Ye, L.; Zhang, S.; Zhao, W.; Yao, H.; Hou, J. Highly Efficient 2D-Conjugated Benzodithiophene-Based Photovoltaic Polymer with Linear Alkylthio Side Chain. *Chem. Mater.* **2014**, *26*, 3603−3605.

(13) Liu, Y.; Zhao, J.; Li, Z.; Mu, C.; Ma, W.; Hu, H.; Jiang, K.; Lin, H.; Ade, H.; Yan, H. Aggregation and Morphology Control Enables Multiple Cases of High-Efficiency Polymer Solar Cells. *Nat. Commun.* **2014**, *5*, 5293/1−8.

(14) Delgado, J. L.; Bouit, P.-A.; Filippone, S.; Herranz, M. A.; Martín, N. Organic Photovoltaics: A Chemical Approach. *Chem. Commun.* **2010**, *46*, 4853−4865.

(15) Li, C.-Z.; Yip, H.-L.; Jen, A. K. -Y. Functional Fullerenes for Organic Photovoltaics. *J. Mater. Chem.* **2012**, *22*, 4161−4177.

(16) Matsuo, Y. Design Concept for High-LUMO-Level Fullerene Electron-acceptors for Organic Solar Cells. *Chem. Lett.* **2012**, *41*, 754−759.

(17) Li, Y. Fullerene-Bisadduct Acceptors for Polymer Solar Cells. *Chem.—Asian J.* **2013**, *8*, 2316−2328.

(18) Zhao, G.; He, Y.; Li, Y. 6.5% Efficiency of Polymer Solar Cells Based on Poly(3-hexylthiophene) and Indene-C60 Bisadduct by Device Optimization. *Adv. Mater.* **2010**, *22*, 4355−4358.

(19) Kim, K.-H.; Kang, H.; Nam, S. Y.; Jung, J.; Kim, P. S.; Cho, C.-H.; Lee, C.; Yoon, S. C.; Kim, B. J. Facile Synthesis of o-Xylenyl Fullerene Multiadducts for High Open Circuit Voltage and Efficient Polymer Solar Cells. *Chem. Mater.* **2011**, *23*, 5090−5095.

(20) Kang, H.; Cho, C.-H.; Cho, H.-H.; Kang, T. E.; Kim, H. J.; Kim, K.-H.; Yoon, S. C.; Kim, B. J. Controlling Number of Indene Solubilizing Groups in Multiadduct Fullerenes for Tuning Optoelectronic Properties and Open-Circuit Voltage in Organic Solar Cells. *ACS Appl. Mater. Interfaces* **2012**, *4*, 110−116.

(21) Matsuo, Y.; Kawai, J.; Inada, H.; Nakagawa, T.; Ota, H.; Otsubo, S.; Nakamura, E. Addition of Dihydromethano Group to Fullerenes to Improve the Performance of Bulk Heterojunction Organic Solar Cells. *Adv. Mater.* **2013**, *25*, 6266−6269.

(22) He, D.; Du, X.; Xiao, Z.; Ding, L. Methanofullerenes, $C_{60}(CH_2)_n$ (n = 1, 2, 3), as Building Blocks for High-Performance Acceptors Used in Organic Solar Cells. *Org. Lett.* **2014**, *16*, 612−615.

(23) Kitaura, S.; Kurotobi, K.; Sato, M.; Takano, Y.; Umeyama, T.; Imahori, H. Effects of Dihydronaphthyl-Based [60]Fullerene Bisadduct Regioisomers on Polymer Solar Cell Performance. *Chem. Commun.* **2012**, *48*, 8550−8552.

(24) Meng, X.; Zhao, G.; Xu, Q.; Tan, Z.; Zhang, Z.; Jiang, L.; Shu, C.; Wang, C.; Li, Y. Effects of Fullerene Bisadduct Regioisomers on Photovoltaic Performance. *Adv. Funct. Mater.* **2014**, *24*, 158−163.

(25) Williams, M.; Tummala, N. R.; Aziz, S. G.; Risko, C.; Brédas, J.-L. Influence of Molecular Shape on Solid-State Packing in Disordered $PC_{61}BM$ and $PC_{71}BM$ Fullerenes. *J. Phys. Chem. Lett.* **2014**, *5*, 3427−3433.

(26) Xiao, Z.; Matsuo, Y.; Soga, I.; Nakamura, E. Structurally Defined High-LUMO-Level 66π-[70]Fullerene Derivatives: Synthesis and Application in Organic Photovoltaic Cells. *Chem. Mater.* **2012**, *24*, 2572−2582.

(27) Wong, W. W. H.; Subbiah, J.; White, J. M.; Seyler, H.; Zhang, B.; Jones, D. J.; Holmes, A. B. Single Isomer of Indene-C_{70} Bisadduct−Isolation and Performance in Bulk Heterojunction Solar Cells. *Chem. Mater.* **2014**, *26*, 1686−1689.

(28) Bouwer, R. K. M.; Hummelen, J. C. The Use of Tethered Addends to Decrease the Number of Isomers of Bisadduct Analogues of PCBM. *Chem.—Eur. J.* **2010**, *16*, 11250−11253.

(29) Delgado, J. L.; Martín, N.; de la Cruz, P.; Langa, F. Pyrazolinofullerenes: a Less Known Type of Highly Versatile Fullerene Derivatives. *Chem. Soc. Rev.* **2011**, *40*, 5232−5241.

(30) Liao, M.-H.; Lai, Y.-Y.; Lai, Y.-Y.; Chen, Y.-T.; Tsai, C.-E.; Liang, W.-W.; Cheng, Y.-J. Synthesis of Mono- and Bisadducts of Thieno-o-quinodimethane with C_{60} for Efficient Polymer Solar Cells. *ACS Appl. Mater. Interfaces* **2014**, *6*, 996−1004.

(31) Hoke, E. T.; Vandewal, K.; Bartelt, J. A.; Mateker, W. R.; Douglas, J. D.; Noriega, R.; Graham, K. R.; Fréchet, J. M. J.; Salleo, A.; McGehee, M. D. Recombination in Polymer:Fullerene Solar Cells with Open-Circuit Voltages Approaching and Exceeding 1.0 V. *Adv. Energy Mater.* **2013**, *3*, 220−230.

(32) Mikie, T.; Saeki, A.; Masuda, H.; Ikuma, N.; Kokubo, K.; Seki, S. New Efficient (Thio)acetalized Fullerene Monoadducts for Organic Solar Cells: Characterization Based on Solubility, Mobility Balance, and Dark Current. *J. Mater. Chem. A* **2015**, *3*, 1152−1157.

(33) Filippone, S.; Maroto, E. E.; Martín-Domenech, E.; Suarez, M.; Martín, N. An Efficient Approach to Chiral Fullerene Derivatives by Catalytic Enantioselective 1,3-Dipolar Cycloadditions. *Nat. Chem.* **2009**, *1*, 578−582.

(34) Maroto, E. E.; Izquierdo, M.; Reboredo, S.; Marco-Martínez, J.; Filippone, S.; Martín, N. Chiral Fullerenes from Asymmetric Catalysis. *Acc. Chem. Res.* **2014**, *47*, 2660−2670.

(35) Kokubo, K.; Masuda, H.; Ikuma, N.; Mikie, T.; Oshima, T. Synthesis and Characterization of New Acetalized [60]Fullerenes. *Tetrahedron Lett.* **2013**, *54*, 3510−3513.

(36) Bitzer, R. S.; Barbosa, A. G. H.; da Silvac, C. O.; Nascimento, M. A. C. On the Generalized Valence Bond Description of the Anomeric and Exo-Anomeric Effects: An ab initio Conformational Study of 2-Methoxytetrahydropyran. *Carbohydr. Res.* **2005**, *340*, 2171−2184.

(37) Takahashi, O.; Yamasaki, K.; Kohno, Y.; Ohtaki, R.; Ueda, K.; Suezawa, H.; Umezawa, Y.; Nishio, M. The Anomeric Effect Revisited. A Possible Role of the CH/n Hydrogen Bond. *Carbohydr. Res.* **2007**, *342*, 1202−1209.

(38) Takahashi, O.; Yamasaki, K.; Kohno, Y.; Ueda, K.; Suezawa, H.; Nishio, M. The Origin of the Generalized Anomeric Effect: Possibility of CH/n and CH/π Hydrogen Bonds. *Carbohydr. Res.* **2009**, *344*, 1225−1229.

(39) Harabe, T.; Matsumoto, T.; Shioiri, T. Esters of 2,5-Multisubstituted-1,3-Dioxane-2-Carboxylic Acid: Their Conformational Analysis and Selective Hydrolysis. *Tetrahedron* **2009**, *65*, 4044−4052.

(40) Mikie, T.; Saeki, A.; Ikuma, N.; Kokubo, K.; Seki, S. Spiro-1,3-dioxolanofullerenes with Low-lying LUMO Level for Organic Solar Cells. *Chem. Lett.* **2015**, *44*, 282−284.

(41) The detailed data are summarized in the Supporting Information and CIF file (CCDC 1044422). A single crystal of *exo-PhSAF₆*·CDCl₃·CS₂ was obtained from toluene solution. The approximate crystal dimensions were 0.30 × 0.20 × 0.15 mm³, T = −150 °C. Crystal data: $C_{73}H_{16}O_2$·CDCl₃·CS₂ M = 1121.44, orthorhombic, a = 10.1777(2) Å, b = 13.4039(3) Å, c = 17.3044(4) Å, V = 2183.72(7) Å³, P-1 (#2), Z = 2, D_{calc} = 1.704 g cm⁻³, μ (Cu K$_α$) = 32.990 cm⁻¹, R = 0.0565.

(42) Lilliu, S.; Agostinelli, T.; Pires, E.; Hampton, M.; Nelson, J.; Macdonald, J. E. Dynamics of Crystallization and Disorder during Annealing of P3HT/PCBM Bulk Heterojunctions. *Macromolecules* **2011**, *44*, 2725−2734.

(43) Saeki, A.; Tsuji, M.; Seki, S. Direct Evaluation of Intrinsic Optoelectronic Performance of Organic Photovoltaic Cells with Minimizing Impurity and Degradation Effects. *Adv. Energy Mater.* **2011**, *1*, 661−669.

(44) Troshin, P. A.; Hoppe, H.; Renz, J.; Egginger, M.; Mayorova, J. Y.; Goryachev, A. E.; Peregudov, A. S.; Lyubovskaya, R. N.; Gobsch, G.; Sariciftci, N. S.; Razumov, V. F. Material Solubility-Photovoltaic Performance Relationship in the Design of Novel Fullerene Derivatives for Bulk Heterojunction Solar Cells. *Adv. Funct. Mater.* **2009**, *19*, 779−788.

(45) Blom, P. W. M.; de Jong, M. J. M.; Vleggaar, J. J. M. Electron and Hole Transport in Poly(p-phenylene vinylene) Devices. *Appl. Phys. Lett.* **1996**, *68*, 3308−3310.

(46) Melzer, C.; Koop, E. J.; Mihailetchi, V. D.; Blom, P. W. M. Hole Transport in Poly(phenylene vinylene)/Methanofullerene Bulk-Heterojunction Solar Cells. *Adv. Funct. Mater.* **2004**, *14*, 865−870.

(47) Dunlap, D. H.; Parris, P. E.; Kenkre, V. M. Charge-Dipole Model for the Universal Field Dependence of Mobilities in Molecularly Doped Polymers. *Phys. Rev. Lett.* **1996**, *77*, 542−545.

(48) Kotlarski, J. D.; Blom, P. W. M. Impact of Unbalanced Charge Transport on the Efficiency of Normal and Inverted Solar Cells. *Appl. Phys. Lett.* **2012**, *100*, 013306/1−3.